

Article

Melting Heat Transfer Rheology in Bioconvection Cross Nanofluid Flow Confined by a Symmetrical Cylindrical Channel with Thermal Conductivity and Swimming Microbes

Fuad A. Awwad ^{1,*} , Emad A. A. Ismail ¹ , Taza Gul ^{2,3,*} , Waris Khan ⁴  and Ishtiaq Ali ⁵ 

¹ Department of Quantitative Analysis, College of Business Administration, King Saud University, P.O. Box 71115, Riyadh 11587, Saudi Arabia; emadali@ksu.edu.sa

² Cambridge Graphene Center, University of Cambridge, 9 JJ Thomson Ave, Cambridge CB3 0FA, UK

³ Department of Mathematics, City University of Science and Information Technology, Peshawar 25000, Pakistan

⁴ Department of Mathematics & Statistics, Hazara University, Mansehra 12120, Pakistan; wariskhan758@yahoo.com

⁵ Department of Mathematics, Comsats University Islamabad, Islamabad 45550, Pakistan; iamirzada@kfu.edu.sa

* Correspondence: fawwad@ksu.edu.sa (F.A.A.); tazagul@cusit.edu.pk (T.G.)

Abstract: Nonlinear thermal transport of non-Newtonian polymer flows is an increasingly important area in materials engineering. Motivated by new developments in this area which entail more refined and more mathematical frameworks, the present analysis investigates the boundary-layer approximation and heat transfer persuaded by a symmetrical cylindrical surface positioned horizontally. To simulate thermal relaxation impacts, the bioconvection Cross nanofluid flow Buongiorno model is deployed. The study examines the magnetic field effect applied to the nanofluid using the heat generated, as well as the melting phenomenon. The nonlinear effect of thermosolutal buoyant forces is incorporated into the proposed model. The novel mathematical equations include thermophoresis and Brownian diffusion effects. Via robust transformation techniques, the primitive resulting partial equations for momentum, energy, concentration, and motile living microorganisms are rendered into nonlinear ordinary equations with convective boundary postulates. An explicit and efficient numerical solver procedure in the Mathematica 11.0 programming platform is developed to engage the nonlinear equations. The effects of multiple governing parameters on dimensionless fluid profiles is examined using plotted visuals and tables. Finally, outcomes related to the surface drag force, heat, and mass transfer coefficients for different influential parameters are presented using 3D visuals.

Keywords: symmetrical cylinder; nanofluid; numerical platform; bioconvection; swimming microbes; melting heat transfer



Citation: Awwad, F.A.; Ismail, E.A.A.; Gul, T.; Khan, W.; Ali, I. Melting Heat Transfer Rheology in Bioconvection Cross Nanofluid Flow Confined by a Symmetrical Cylindrical Channel with Thermal Conductivity and Swimming Microbes. *Symmetry* **2023**, *15*, 1647. <https://doi.org/10.3390/sym15091647>

Academic Editors: Ranjit Kumar Upadhyay and Ramalingam Udhayakumar

Received: 20 July 2023

Revised: 18 August 2023

Accepted: 21 August 2023

Published: 25 August 2023



Copyright: © 2023 by the authors. Licensee MDPI, Basel, Switzerland. This article is an open access article distributed under the terms and conditions of the Creative Commons Attribution (CC BY) license (<https://creativecommons.org/licenses/by/4.0/>).

1. Introduction

Several researchers have conducted investigations into the thermophysical importance of nanoparticles. Nanofluids are formed by mixing nanomaterials and a base liquid, with the suspensions consisting of various metals or nonmetals, such as aluminum, copper, silver, and graphite, and water, glycerol, and ethylene glycol being used as base liquids. Nanofluids play an important role in various processes, such as polymer, wire-coating, and biomedical processes. These processes are used in heat transportation, nuclear reactors, and electronic devices, as well as in medical applications such as the diagnosis and treatment of several diseases. Ferrofluids, which are a special type of magnetized fluid, have significant applications in various engineering processes such as microfluid pumps, ferrofluid lubrication of bearings, lithographic design, electromechanical and chemical devices, electrical engines, as well as in medicine and in magnet therapy for treating migraines and arthritis, among other conditions [1–5].

The Buongiorno nanofluid model [6] describes two unusual processes to enhance the rate of heat transfer. Venkatadri et al. [7] examined the melting heat exchange between an electrically conductive flow of nanofluid across an exponentially expanding permeable channel with Cattaneo–Christov heat flux in the presence of an external magnetic field.

Mondal et al. [8] explored the effects of MHD flow and heat exchange on the flow of stagnation-point nanofluids over an extended surface with chemical reaction and thermal radiation effect. Ying et al. [9] explored the radiative heat transfers of molten salt-based nanofluids over cooling coils with non-uniform heat flow. Zainal et al. [10] monitored the MHD hybrid nanofluid stream to a porous expanding/shrinking channel with the emergence of quadratic momentum. Eid et al. [11] studied the variable thermal conductivity effect and heat transfer phenomena on an MHD flow of nanofluid across a porous channel with velocity slip. Many researchers have used the Buongiorno model to study nanofluids, as evidenced by references [12–19]. Kamal et al. [20] conducted an analytical investigation of a viscoelastic nanofluid with a twofold diffusion problem resulting from the stagnation-point flow induced by heat transfer in a space environment. Anuar et al. [21] investigated the numerical solution of the stagnation-point flow and the heat transfer analysis of radiative Maxwell hybrid nanofluids over a nonlinear stretching channel. Rizwana et al. [22] examined the slip effects on radiative oblique stagnation-point nanofluid with convective heat-transfer effect in the presence of the inclined magnetic field. In their research, Giri et al. [23] investigated the nanoparticle diameter effect and the interfacial layer effect on the MHD flow of nanofluid and the melting heat flow inside a rotating plate channel positioned horizontally. Meanwhile, Sharma et al. [24] studied the impact of variable thickness and melting heat exchange on the flow of MHD nanofluids through a slender elongated surface. Bioconvection is a phenomenon in which microorganisms swim upwards in less dense fluids than water, resulting in an increased concentration of microorganisms at the upper layer, leading to breakdowns due to the frailty of the substances. Microorganisms like bacteria or algae use this up-swimming technique for their growth and development. The bioconvection process has various applications in biochemistry and bioengineering, including diesel-fuel products, bioreactors, and fuel-cell engineering, making it an important field in biomedical engineering. The discovery of the bioconvection phenomenon is attributed to Platt [25], while Kuznetsov [26] is believed to have been the first to use the term “nanofluid bioconvection.” Kuznetsov [27] further developed this concept by focusing on the role of gyrotactic motile microorganisms in nanofluids and demonstrating that the large-scale fluid movement generated by these self-propelled microorganisms improves mixing and prevents nanomaterial buildup in nanofluids. In their study, Haq et al. [28] considered the flow properties of the natural bioconvective process of nanofluid flow with living gyrotactic microbes under the influence of a uniform magnetic field and the Arrhenius activation energy effect. Ahmad et al. [29] explored the bioconvection nanofluid flow of gyrotactic motile bacteria with chemical reactions in a porous medium over a stretched surface. Finally, Elanchezhian et al. [30] studied the heat and mass transfer of an Oldroyd-B mixed bioconvection flow of nanofluid using a stratified medium containing swimming microorganisms and nanoparticles under the influence of an inclined magnetic field. In a study by Bhatti et al. [31], a theoretical investigation was carried out on living microbes in a blood-based nanofluid flow through anisotropically tapered arteries. Khan et al. [32] studied important aspects of activation energy and effective Prandtl number in Jeffrey nanofluid flow containing gyrotactic living microorganisms. Shafiq et al. [33] investigated heat and mass flow in second-grade bioconvective flow with buoyancy effect and first-order chemical reaction. Kotnurkar et al. [34] studied the bioconvective peristaltic flow of a nanofluid containing microorganisms in the presence of Cu-blood nanoparticles across a permeable channel. Muhammad et al. [35] established the impact of time-dependent bioconvection magnetized Carreau fluid flow under the velocity slip effect in the presence of motile microorganisms. Farooq et al. [36] introduced the effect of thermally radioactive bioconvection flow of Carreau fluid in the

presence of Cattaneo–Christov heat flux and an exponential space-based heat source over a stretching cylinder under the influence of magnetic effect. Hosseinzadeh et al. [37] investigated cross-fluid flow containing living microbes and tiny particles through a 3D stretching cylinder. Heat transfer analysis in non-Newtonian fluids is more important in applications such as drug delivery or heat optimization [38,39]. This concept is also of more interest in the case of nanofluids/hybrid nanofluids for enhancing the heat transfer rate of traditional fluids [40,41].

Other important theoretical and experimental studies recently carried out on bioconvection involving living microorganisms have been explored analytically by various researchers and can be viewed in citations [42–48].

These studies cite the fact that no survey has yet been offered on 2D bioconvective Cross nanofluid flow in the presence of living motile microbes along a cylindrical channel positioned horizontally and subject to melting heat rheology and convective boundary conditions. The present analysis aims to introduce an effective mathematical description of the crossflow of nanofluid along the cylindrical channel. The impact of Brownian diffusion and the thermophoresis phenomenon are invoked simultaneously to make consideration of the problem more efficient. The following are the precise goals of this numerical evaluation:

- To study the impact on time-dependent 2D bioconvective Cross nanofluid flow over a cylindrical surface subject to living microbes, thermal conductivity, and melting phenomenon.
- To create a mathematical model of the nonlinear governing PDEs which comprises momentum, temperature gradients, mass balances, and swimming microorganisms.
- To engage numerical techniques for attaining the computational outcomes and, additionally, to produce a convergence and stability analysis for optimizing flow fields.
- To unveil graphical profiles of the effects of diverse emerging parameters on flow fields together with 3D visuals of skin friction, heat transfer, and mass flow coefficients.

Novelty

The novelty of the present study can be summarized as follows:

- The existing literature [48] is extended by including mixed convection in Equation (5).
- The study of microorganisms referred to in Equation (10) is the main novelty of the existing literature [48].
- The present model includes an extension of the melting heat transfer phenomenon, which is stated in Equation (12).
- Statistical analysis of the variation in the values of parameters is also included.

2. Flow Analysis and Mathematical Setup

In this mathematical model, we include the influence of thermal conductivity on the viscous 2D bioconvective flow of a Cross nanofluid bounded by a symmetrical cylindrical surface with the melting phenomenon and in the presence of motile living microbes. Aspects of nonlinear thermal radiation and convective boundary conditions are invoked. The impact of Brownian diffusion and thermophoresis deposition processes are retained in the proposed model. The ambient temperature, nanoparticle volume fraction, and motile microorganisms are signified as T_{∞}^* , C_{∞}^* , and N_{∞}^* . The implications of the induced magnetic field and external electric field are ignored due to the small Reynolds number. The physical scenario can be seen in Figure 1a.

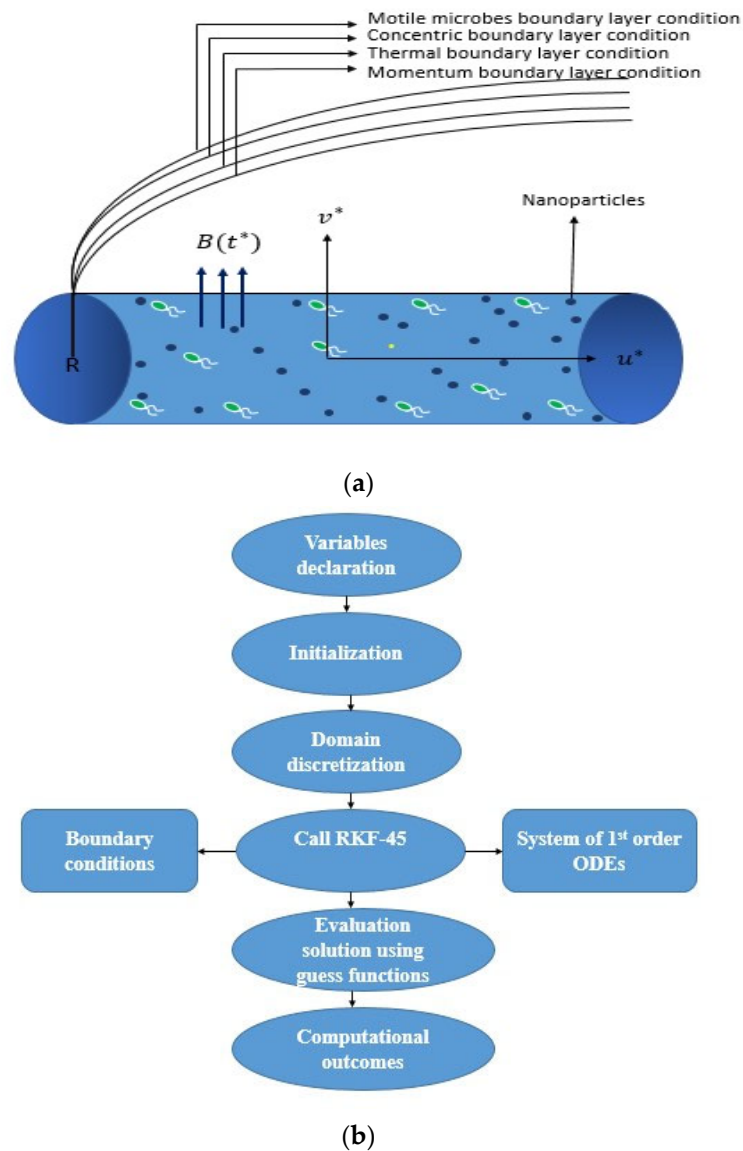


Figure 1. (a) Physical configuration and coordinates; (b) computational flow chart.

Under the above conditions, the boundary-layer approximation yields the following governing equations [33,34]:

$$\tau = -pI + \mu A_1, \mu = \mu_\infty + (\mu_0 + \mu_\infty) / (1 + (\Gamma\bar{\gamma})^n) \tag{1}$$

where

$$A_1 = gradV + (gradV)^t, \bar{\gamma} = \sqrt{0.5(trA_1)^2}$$

Herein, V is the velocity, and the shear rate is zero at infinity; accordingly, Equation (1) may be rewritten as:

$$\mu = \mu_0(1/1 + (\Gamma\bar{\gamma})^n) \tag{2}$$

For 2D unsteady flow, the momentum, temperature gradient, concentration balance, and living microbes are as follows:

$$V = (u^*, v^*), T^* = T^*(r^*, x^*, t^*), C^* = C^*(r^*, x^*, t^*) \tag{3}$$

Substituting Equation (3) in Equations (1)–(2), the resulting equations are as follows [44]:

$$r^* \frac{\partial u^*}{\partial x^*} + r^* \frac{\partial v^*}{\partial r^*} = 0 \tag{4}$$

$$\begin{aligned} \frac{\partial u^*}{\partial t^*} + u^* \frac{\partial u^*}{\partial x^*} + v^* \frac{\partial u^*}{\partial r^*} &= \frac{\partial U_e}{\partial t^*} + U_e \frac{\partial}{\partial z^*} U_e + \frac{v}{r^*} \frac{\partial u^*}{\partial r^*} \left(\frac{1}{1 + (\Gamma \frac{\partial u^*}{\partial r^*})^n} \right) + v \frac{\partial}{\partial t^*} \left(\frac{\frac{\partial u^*}{\partial r^*}}{1 + (\Gamma \frac{\partial u^*}{\partial r^*})^n} \right) - \\ &\frac{1}{\rho_f} \sigma B^2 (t^*) (u^* - U_e) + \beta^* g (1 - C_f^*) (T^* - T_\infty^*) - \frac{g}{\rho_f} (\rho_p - \rho_f) (C^* - C_\infty^*) \\ &- \frac{g \bar{\gamma}}{\rho_f} (\rho_m - \rho_f) (N^* - N_\infty^*) \end{aligned} \tag{5}$$

$$\begin{aligned} \frac{\partial T^*}{\partial t^*} + u^* \left(\frac{\partial T^*}{\partial x^*} \right) + v^* \left(\frac{\partial T^*}{\partial r^*} \right) &= \frac{1}{r^* (\rho c)_f} \frac{\partial}{\partial r^*} \left(r^* K(T^*) \frac{\partial T^*}{\partial r^*} \right) + \frac{1}{r^* (\rho c)_f} \frac{\partial}{\partial r^*} \left(\alpha r^* \frac{\partial T^*}{\partial r^*} \right) + \\ \tau \left(D_B \frac{\partial C^*}{\partial r^*} \frac{\partial T^*}{\partial r^*} + \frac{D_T}{T_\infty^*} \left(\frac{\partial T^*}{\partial r^*} \right)^2 \right) &- \frac{\partial}{\partial r^*} \left(\frac{1}{(\rho c)_f} \frac{16\sigma^*}{3k^*} T^{*3} \frac{\partial T^*}{\partial r^*} \right) \end{aligned} \tag{6}$$

$$K(T^*) = \left(1 + \epsilon \frac{T^* - T_\infty^*}{\Delta T^*} \right) k_\infty \tag{7}$$

$$\frac{\partial C^*}{\partial t^*} + u^* \frac{\partial C^*}{\partial x^*} + v^* \frac{\partial C^*}{\partial r^*} = \frac{1}{(\rho c)_f} \frac{\partial}{\partial r^*} \left[D(T^*) \frac{\partial C^*}{\partial r^*} \right] + \frac{D_B}{r^*} \frac{\partial}{\partial r^*} \left[r^* \frac{\partial C^*}{\partial r^*} \right] + \frac{D_{T^*}}{T_\infty^*} \frac{1}{r^*} \frac{\partial}{\partial r^*} \left[r^* \frac{\partial T^*}{\partial r^*} \right] \tag{8}$$

$$D(C^*) = \left(1 + \epsilon_1 \frac{C^* - C_\infty^*}{\Delta C^*} \right) D_\infty \tag{9}$$

$$\frac{\partial N^*}{\partial t^*} + u^* \left(\frac{\partial N^*}{\partial x^*} \right) + v^* \left(\frac{\partial N^*}{\partial r^*} \right) = D_m \left(\frac{\partial^2 N^*}{\partial r^{*2}} \right) - \left(\frac{b W_c}{C_w^* - C_\infty^*} \right) \frac{\partial}{\partial r^*} \left(N^* \frac{\partial C^*}{\partial r^*} \right) \tag{10}$$

The corresponding boundary postulates for the proposed problem are as given below [44]:

$$\begin{aligned} u^* = u_w(x^*, t^*), v^* = 0, -k_f \frac{\partial T^*}{\partial r^*} = h_f(T^* - T_w), D_B \frac{\partial C^*}{\partial r^*} + \frac{D_{T^*}}{T_\infty^*} \frac{\partial T^*}{\partial r^*} = 0, N^* = N_w^* \text{ at } r^* = R \\ u^* \rightarrow 0, T^* \rightarrow T_\infty^*, C^* \rightarrow C_\infty^*, N^* \rightarrow N_\infty^* \text{ at } r^* \rightarrow \infty \end{aligned} \tag{11}$$

Additionally, the melting heat phenomenon is:

$$k_f \frac{\partial T^*}{\partial r^*} = \rho_f (\lambda^* + (C_p)_s (T_w^* - T_0^*) u^*) \tag{12}$$

For solving the resulting Equations (5)–(11), the dimensionless quantities are implemented as follows:

$$\begin{aligned} \psi = \sqrt{u_w \nu x^*} R u_0^* (\xi), \xi = \sqrt{\frac{u_w}{\nu x^*}} \left(\frac{r^{*2} - R^2}{2R} \right), g(\xi) = \frac{T^* - T_\infty^*}{T_w^* - T_\infty^*}, h(\xi) = \frac{C^* - C_\infty^*}{C_w^* - C_\infty^*}, \\ X(\xi) = \frac{N^* - N_\infty^*}{N_w^* - N_\infty^*} \end{aligned} \tag{13}$$

Thus, the dimensionless forms achieved are as follows:

$$\begin{aligned} \left(1 + (1 - n) (We u_0'')^n \right) (1 + 2\alpha \xi) u_0''' + 2\alpha u_0'' \left(\left(1 + (We u_0'')^n \left(1 - \frac{n}{2} \right) \right) \right) \left(1 + (We u_0'')^n \right)^2 \times \\ \left(Re \left(u_0 u_0'' + u_0''^2 + 1 \right) \right) - A \left(u_0' + \frac{\xi}{2} u_0 u_0'' \right) - M^2 Re (u_0' - 1) + \lambda (g - Nr h - Nc X) = 0 \end{aligned} \tag{14}$$

$$\begin{aligned} \frac{1}{Pr} (1 + 2\alpha \xi) (1 + \epsilon g) g'' + \epsilon \xi (g'')^2 + g' (2\alpha + u_0) - \frac{1}{2} A \xi g' + Nb (1 + 2\alpha \xi) \left(g' h' + \frac{Nt}{Nb} g' \right) + \\ \frac{2}{3PrR} \left((1 + (\theta_w - 1)g)^3 (2\alpha g' + 2g'' (1 + 2\alpha \xi)) + 6(1 + (\theta_w - 1)g)^2 \right) \times \\ (\theta_w - 1) (g'')^2 (1 + 2\alpha \xi) = 0 \end{aligned} \tag{15}$$

$$(1 + 2\alpha\zeta)(1 + \epsilon_2 g)h'' + \epsilon_2 (h')^2 + 2\alpha h' + \text{PrLe} \left(u_0 h' + \frac{Nt}{Nb} ((1 + 2\alpha\zeta)g'' + 2\alpha g') - \frac{1}{2}\zeta h' \right) = 0 \tag{16}$$

$$(1 + 2\alpha\zeta)X'' + (2\alpha + Lbu_0)X' - Pe((\delta_1 + X)h'' + h'X') = 0 \tag{17}$$

The transformed boundary postulates in dimensionless form are as follows:

$$\begin{aligned} u'_0 = 1, g' = -Bi(1 - g), h' + \left(\frac{Nt}{Nb}\right)g' = 0, X = 1 \text{ at } \zeta = 0 \\ u'_0 = 0, g = 0, h = 0, X = 1 \text{ at } \zeta = \infty \end{aligned} \tag{18}$$

where

$$\begin{aligned} \alpha = \frac{1}{R} \sqrt{\frac{\nu l}{U_0}}; M = \frac{\sigma B_0^2}{\rho C_p}; A = \frac{\epsilon}{a}; Nr = \frac{(\rho_p - \rho_f)(C_w^* - C_\infty^*)}{\beta^*(1 - C_\infty^*)(T_w^* - T_\infty^*)}; Nc = \left(\frac{\rho_m - \rho_f}{\beta}\right) \frac{(N_w^* - N_\infty^*)}{(T_w^* - T_\infty^*)(1 - C_\infty^*)} \gamma^{**}; \\ \lambda = \frac{g\nu(1 - C_\infty^*)(T_w^* - T_\infty^*)\beta^*}{u_w}; We = \frac{u_w r^* \Gamma^2 g(1 - C_\infty^*)(T_w^* - T_\infty^*)\beta^*}{(1 - ct^*)^3 \nu}; Pr = \frac{\nu_f}{\alpha}; R = \frac{kk^*}{4\sigma^* T_\infty^{*3}}; \\ Nb = D_B E \frac{(C_w^* - C_\infty^*)}{\alpha}; Nt = D_T E \frac{(T_w^* - T_\infty^*)}{T_\infty^* \alpha}; \theta_w = \frac{T_w^*}{T_\infty^*}; Le = \frac{\alpha}{D_B}; Lb = \frac{\nu}{D_m}; Pe = \frac{bW_c}{D_m}; \\ Ma = \frac{c_p(T_w^* - T_\infty^*)}{\lambda + c_s(T_w^* - T_0^*)}; Bi = \frac{h_f}{k} \sqrt{\frac{\nu_f}{a}} \end{aligned}$$

are curvature parameter, magnetic parameter, time-dependent parameter, buoyancy parameter, Rayleigh number, convection parameter, Weissenberg number, Prandtl number, radiation parameter, Brownian factor, thermophoretic force, ratio parameter, Lewis number, bioconvection Lewis number, Peclet number, melting heat phenomenon, and Biot number, respectively.

The melting phenomenon in dimensionless form is as follows:

$$\text{Pru}_0(0) + \text{Mag}'(0) = 0 \tag{19}$$

The skin fraction, heat transfer coefficient, mass flow rate, and gradients of living microbes are defined as follows:

$$Cf = \frac{\tau_{x^*r^*}}{\rho_f U^2}, Nu = \frac{x^* q_w}{k(T_w^* - T_\infty^*)}, Sh = \frac{x^* q_m}{-D_B(C_w^* - C_\infty^*)}, Nh = \frac{x^* q_j}{-D_B(N_w^* - N_\infty^*)} \tag{20}$$

whereas $\tau_{x^*r^*}$ elucidates shear stress, q_w heat flux, q_m mass flux, and q_j mass of living microbes are characterized in this way:

$$\left. \begin{aligned} \tau_{x^*r^*} &= \mu_0 \frac{\partial u^*}{\partial r^*} \left(\frac{1}{1 + (\Gamma \frac{\partial u^*}{\partial r^*})^n} \right) \\ q_w &= -k(T^*) \frac{\partial T^*}{\partial r^*} \\ q_m &= -D_B \frac{\partial C^*}{\partial r^*} \\ q_j &= -D_B \frac{\partial N^*}{\partial r^*} \end{aligned} \right\}_{r^*=R} \tag{21}$$

Replacing Equation (21) in Equation (20), we get the dimensionless form in Equation (22):

$$\left. \begin{aligned} \sqrt{\text{Re}_x} Cf_x &= u''_0(0) \left(\frac{1}{(1 + (We)u''_0(0))^n} \right) \\ \frac{Nu_x}{\sqrt{\text{Re}_x}} &= -g'(0) \left(1 + \frac{1}{Nr} \left((1 + (\theta_w - 1)g'(0))^3 \right) \right) \\ \frac{Sh_x}{\sqrt{\text{Re}_x}} &= -h'(0) \\ \frac{Nh_x}{\sqrt{\text{Re}_x}} &= -X'(0) \end{aligned} \right\} \tag{22}$$

Here, $\text{Re}_x = \frac{x^* u_w}{\nu}$ is the local Reynolds number.

3. Computational Procedure

In this section, we present the solution of nonlinear differential Equations (14)–(17) subject to the boundary conditions represented in Equation (18). The physical system is engaged numerically through a built-in algorithm/shooting technique (RK-4) in the Mathematica 11.0 programming platform. The nonlinear coupled equations are first diminished towards a system of first-order initial value differential equations using suitable transformation variables [38,46]:

$$\begin{aligned} u_0 &= w_1, u'_0 = w_2, u''_0 = w_3, g = w_4, g' = w_5, h = w_6, h' = w_7, \\ X &= w_8, X' = w_9 \end{aligned} \tag{23}$$

Typically, the RKF45 order technique is applied to solve initial value problems (IVPs), leading to the conversion of equations into their first-order form. In the context of the current approach, these equations are restructured as follows.

By inserting Equation (23) into Equations (14) through (18), we obtain the following system of initial-order equations:

$$w'_3 = \frac{\left(A \left(w_2 + \frac{\xi}{2} w_1 w_3 \right) + M^2 \text{Re}(w_2 - 1) - \lambda(w_4 - Nr w_6 - Nc w_8) - 2\alpha w_3 \left((1 + (We w_3)^n \left(1 - \frac{n}{2} \right) \right) \right) (1 + (We w_3)^n)^2 \times (\text{Re}(w_1 w_3 + w_3^2 + 1))}{(1 + (1 - n)(We w_3)^n) (1 + 2\alpha \xi)} \tag{24}$$

$$u'_5 = \frac{\text{Pr} \left(\frac{g'(2\alpha + w_1) + \frac{1}{2} A \xi w_5 - \epsilon \xi (w'_5)^2 - Nb(1 + 2\alpha \xi) w_5 \left(w_7 + \frac{Nt}{Nb} \right) - \frac{2}{3\text{Pr}R} \left((1 + (\theta_w - 1) w_4)^3 \left(\frac{2\alpha w_5 + 2w'_5(1 + 2\alpha \xi)}{6(1 + (\theta_w - 1) w_4)^2} \right) \right) \times (\theta_w - 1) (w'_5)^2 (1 + 2\alpha \xi)}{(1 + 2\alpha \xi)(1 + \epsilon w_4)} \right)}{(1 + 2\alpha \xi)(1 + \epsilon w_4)} \tag{25}$$

$$w'_7 = - \frac{\left(\epsilon_2 (w_7)^2 + 2\alpha w_7 + \text{Pr}Le \left(\frac{u_0 w_7 + \frac{Nt}{Nb} ((1 + 2\alpha \xi) w'_5 + 2\alpha w_5)}{-\frac{1}{2} \xi w_7} \right) \right)}{(1 + 2\alpha \xi)(1 + \epsilon_2 w_4)} \tag{26}$$

$$w'_9 = \frac{Pe((\delta_1 + w_9)w'_7 + w_7 w_9) - (2\alpha + Lb w_1)w_9}{(1 + 2\alpha \xi)} \tag{27}$$

Following that, the associated boundary criteria are as follows:

$$\begin{aligned} w_2 &= 1, w_5 = -Bi(1 - w_4), w_7 + \left(\frac{Nt}{Nb} \right) w_5 = 0, w_8 = 1 \text{ at } \xi = 0 \\ w_2 &= 0, w_3 = 0, w_6 = 0, w_9 = 1 \text{ at } \xi = \infty \end{aligned} \tag{28}$$

The entire nonlinear computational framework of the shooting technique is described below in Figure 1.

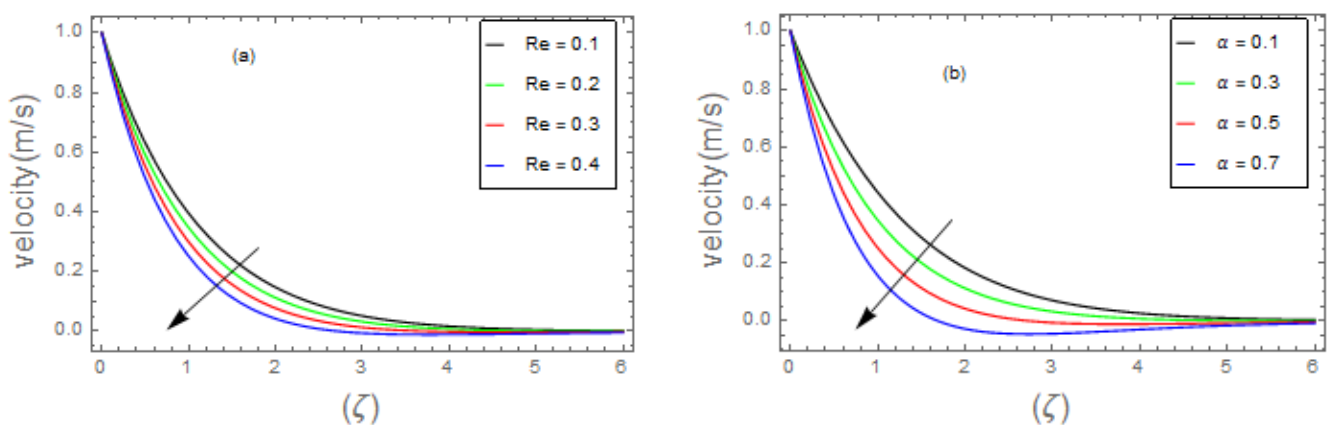
It is important to note that the numerical results derived from solving the governing equations for the problem using the abovementioned RKF45 method have been validated against the findings presented in the work by Ishak et al. [19]. The comparison serves to highlight the exceptional precision of the results obtained through this research effort, as showcased in Table 1.

Table 1. Evaluation of local skin friction coefficients for physical parameters.

M	λ	Nr	Nc	Ref [48]	Present Results
0.1	0.2	0.1	0.1	1.1725	1.17274
0.4				1.2565	1.25682
0.8				1.3024	1.30257
0.5	0.5	0.1	0.1	1.2795	1.27971
	1.0			1.2572	1.25743
	1.5			1.2453	1.24536
0.0	0.2	0.5	0.1	1.2601	1.26028
		1.0		1.2703	1.27053
		1.2		1.2832	1.28396
0.5	0.2	0.1	0.5	1.2865	1.28672
			1.0	1.2902	1.29343
			1.2	1.2974	1.29792

4. Graphical Outcomes

In this section we examine the physical insights into the Cross nanofluid problem as provided by the numerical solution, in which a built-in algorithm allows a computational framework to be obtained by the use of a shooting procedure. These include the action of important parameters on different flow fields, such as flow stream, temperature gradient, concentration, concentration of microbes, skin friction, heat transfer coefficient, and mass flow rate characteristics. The set of nonlinear computational outcomes for fluid velocity profile, temperature gradient, mass concentration, and living microbes within the boundary layer for varying values of dimensionless flow parameters have been computed by the Mathematica 11.0 programming software. The relevant assorted parameters are graphically represented in Figures 2–21.

**Figure 2.** (a,b) u'_0 impacts for various Re and α .

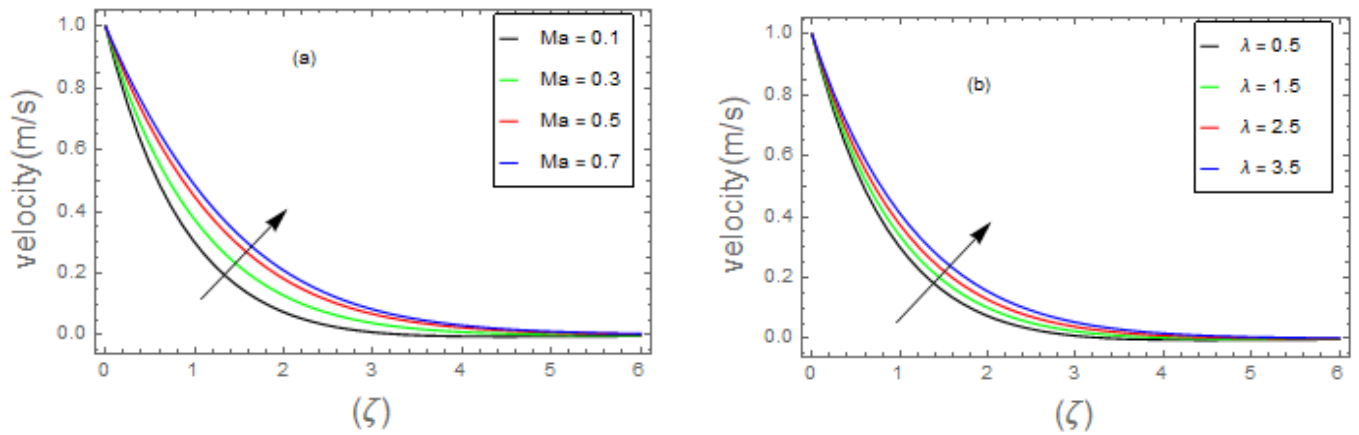


Figure 3. (a,b) u'_0 impacts for various Ma and λ .

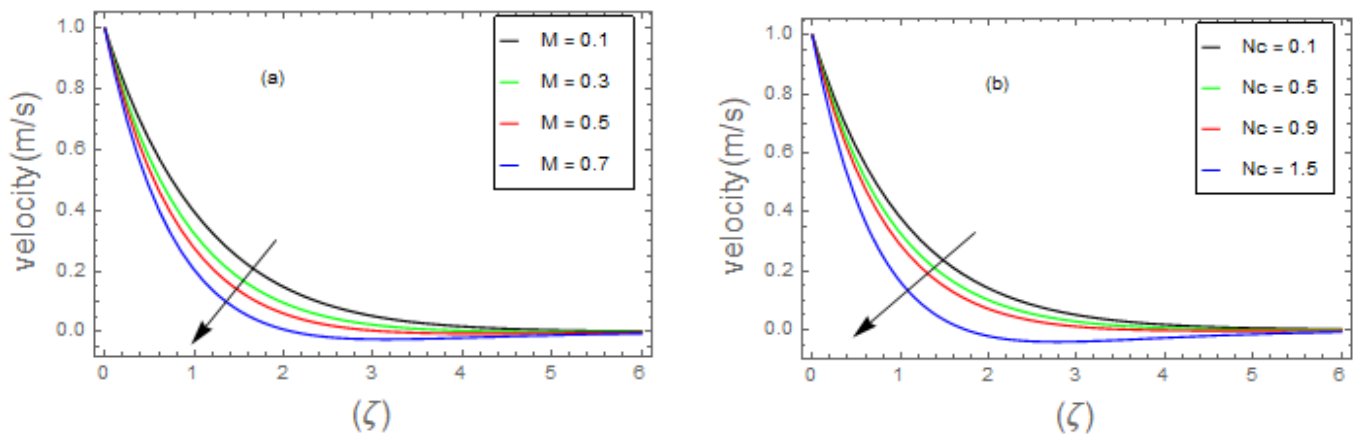


Figure 4. (a,b) u'_0 impacts for various M and Nc .

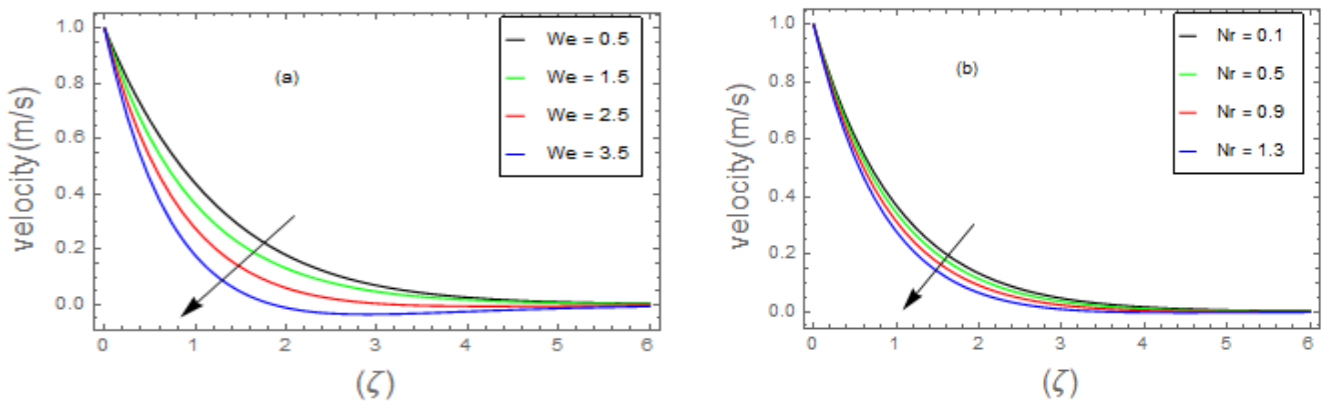


Figure 5. (a,b) u'_0 impacts for various We and Nr .

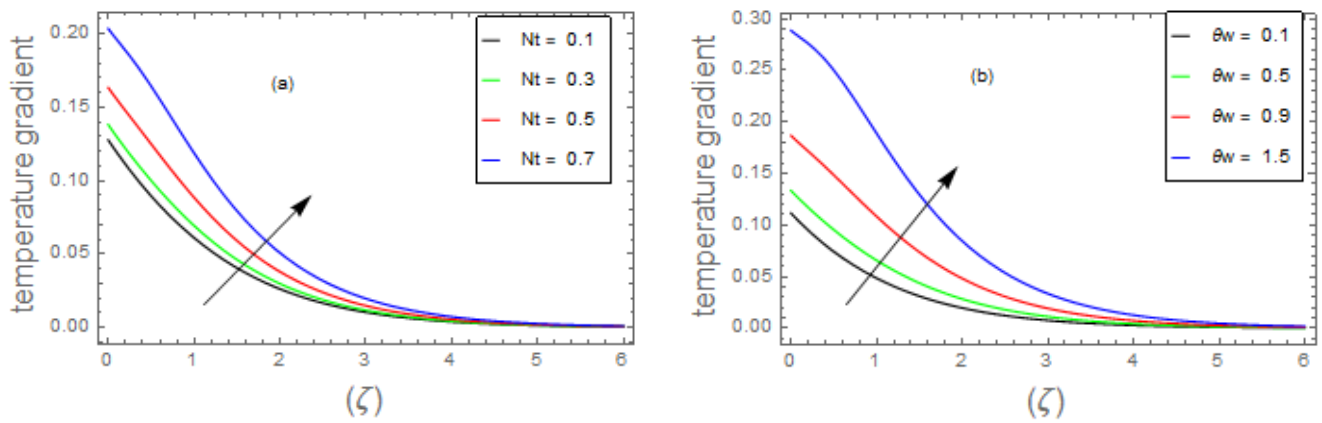


Figure 6. (a,b) $g(\zeta)$ impacts for various Nt and θ_w .

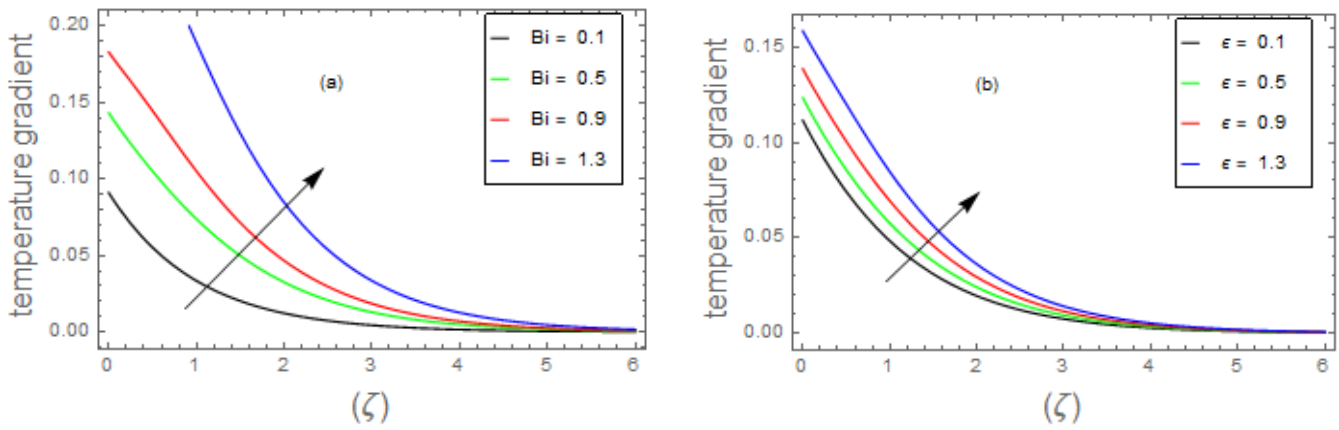


Figure 7. (a,b) $g(\zeta)$ impacts for various Bi and ϵ .

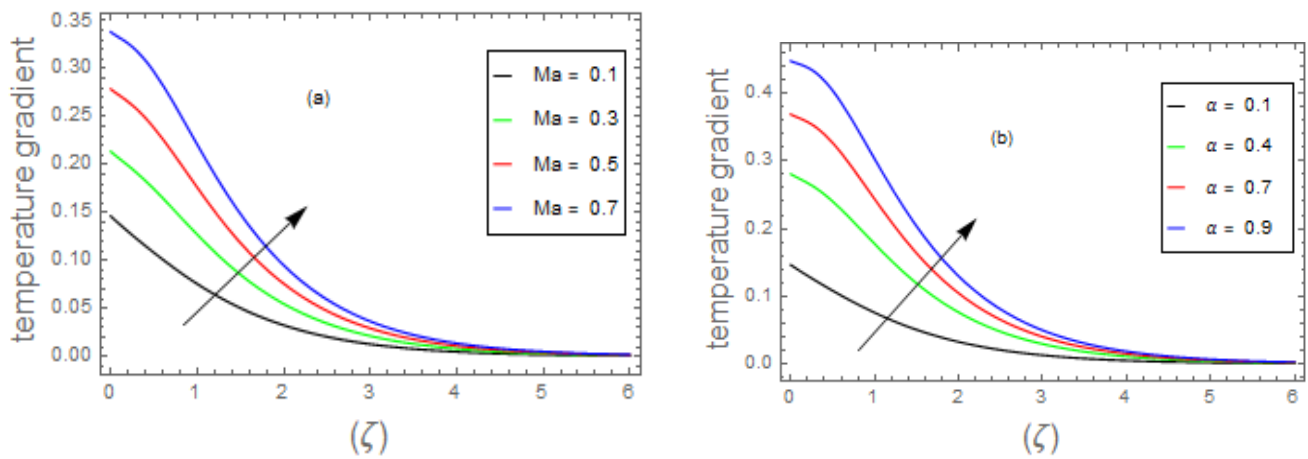


Figure 8. (a,b) $g(\zeta)$ impacts for various Ma and α .

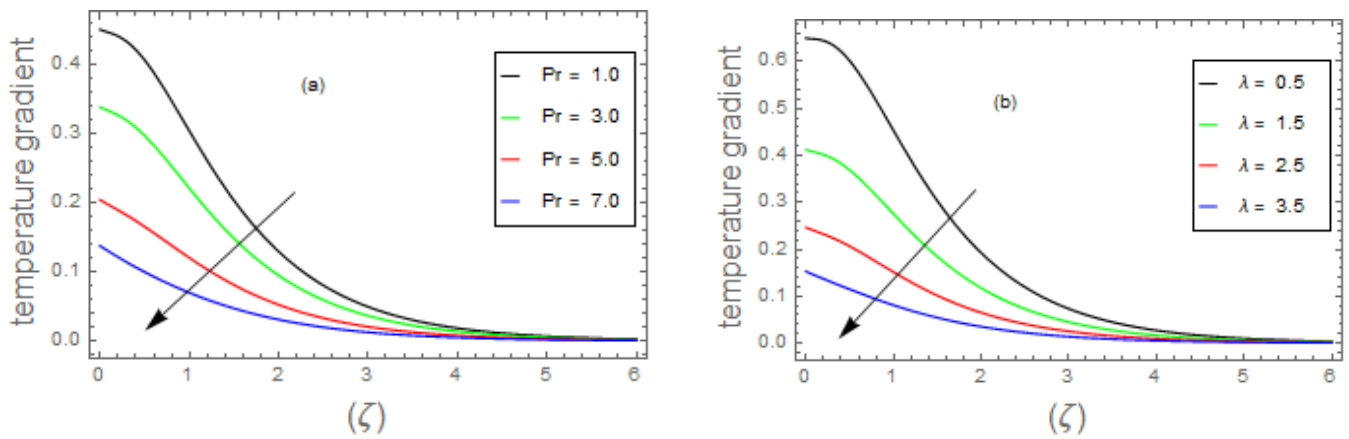


Figure 9. (a,b) $g(\zeta)$ impacts for various Pr and λ .

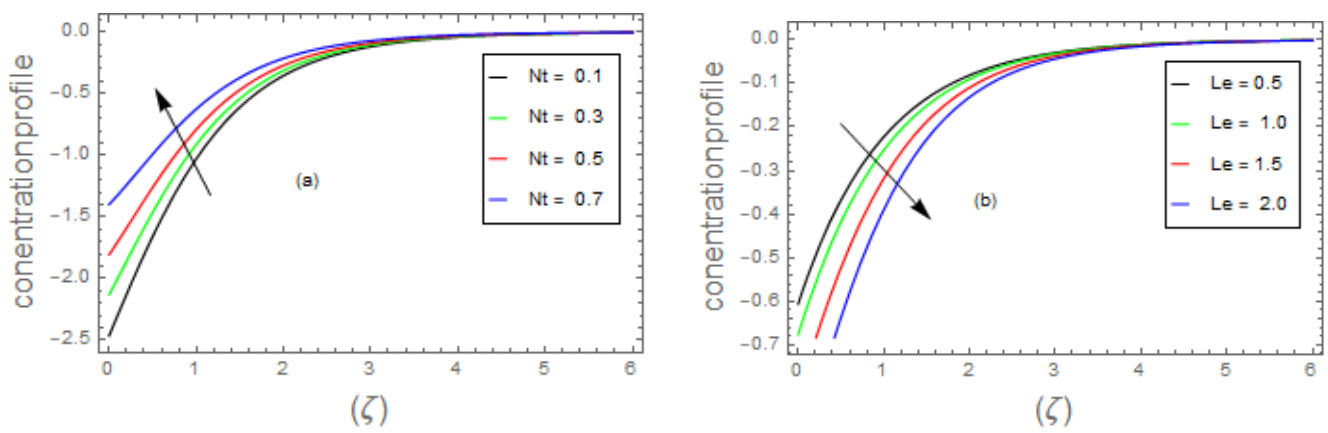


Figure 10. (a,b) $h(\zeta)$ impacts for various Nt and Le.

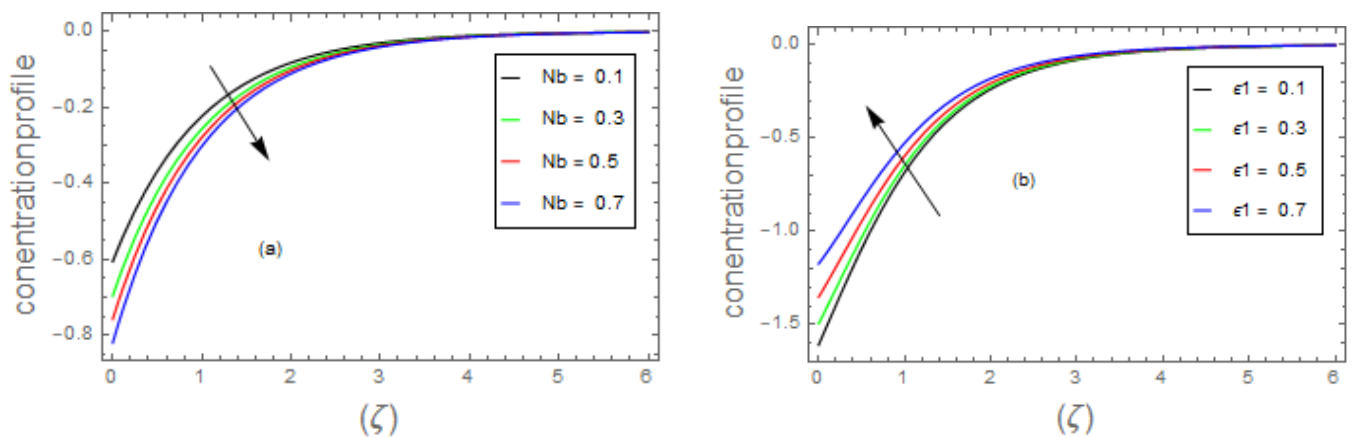


Figure 11. (a,b) $h(\zeta)$ impacts for various Nt and ϵ_1 .

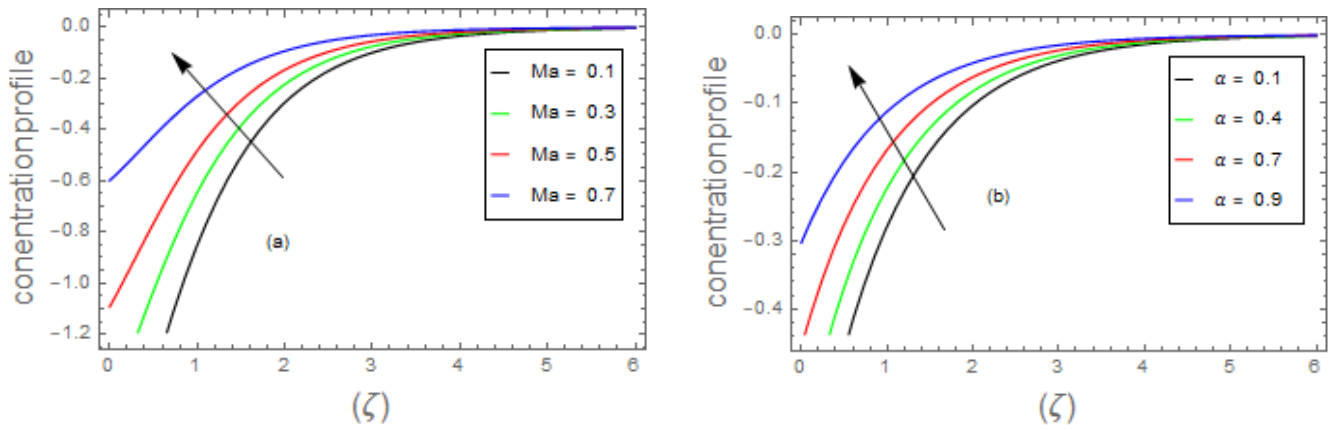


Figure 12. (a,b) $h(\zeta)$ impacts for various Ma and α .

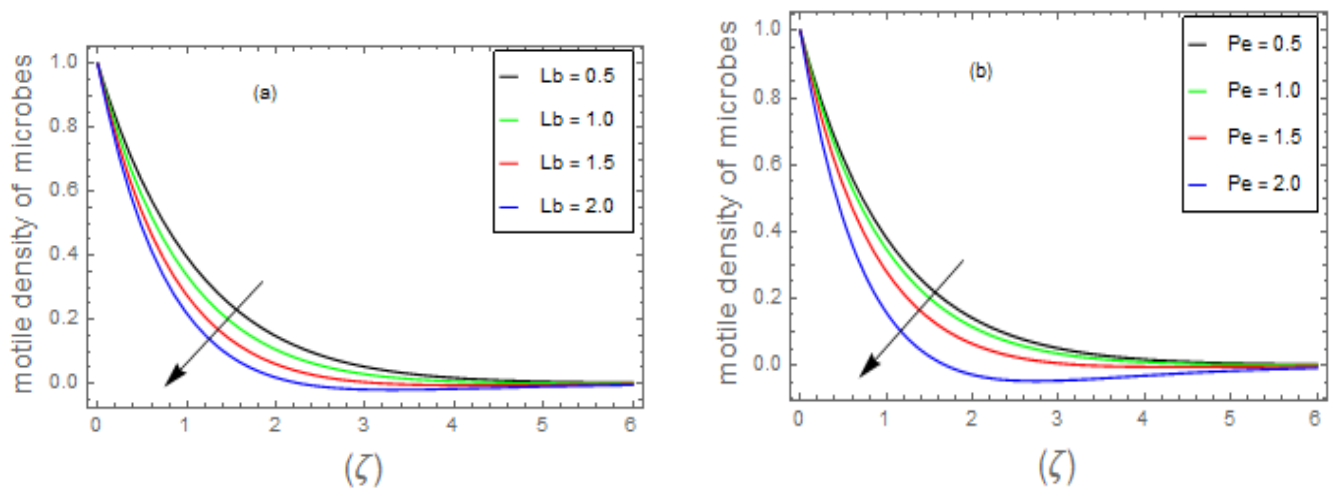


Figure 13. (a,b) $\Upsilon(\zeta)$ impacts for various Lb and Pe .

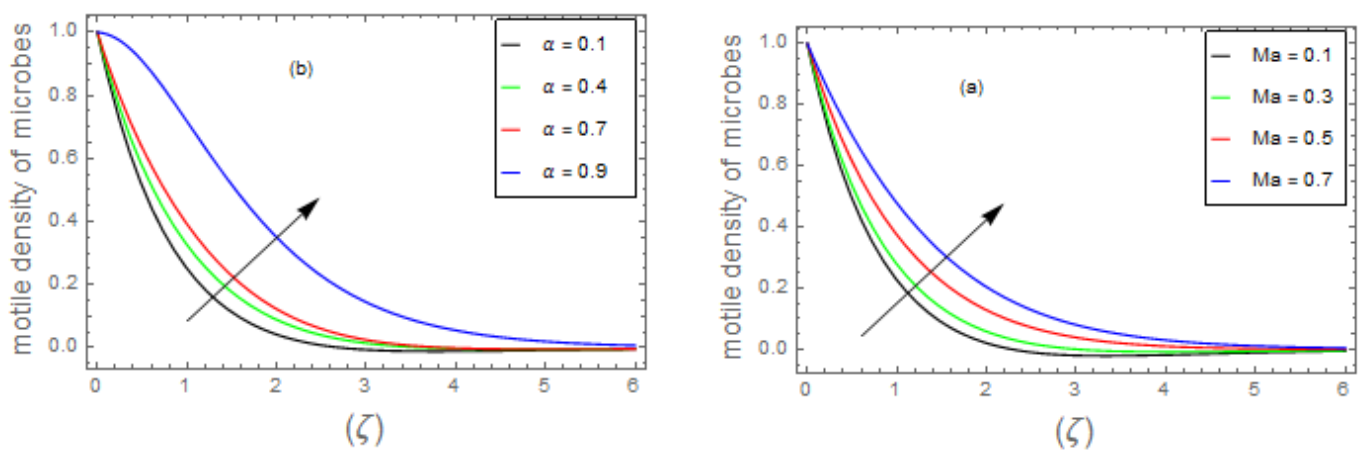


Figure 14. (a,b) $\Upsilon(\zeta)$ impacts for various Ma and α .

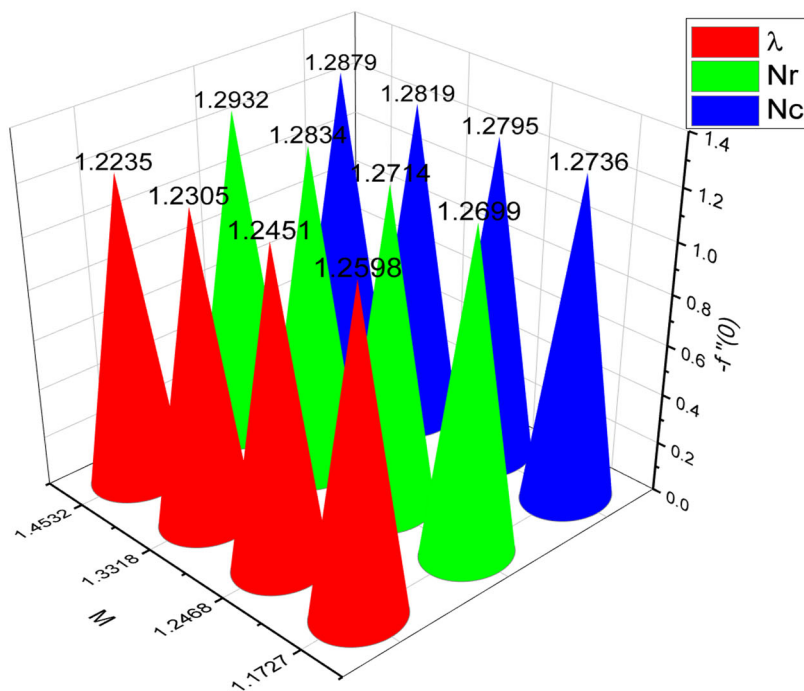


Figure 15. Skin friction estimation via (M, λ, Nr, Nc) parameters.

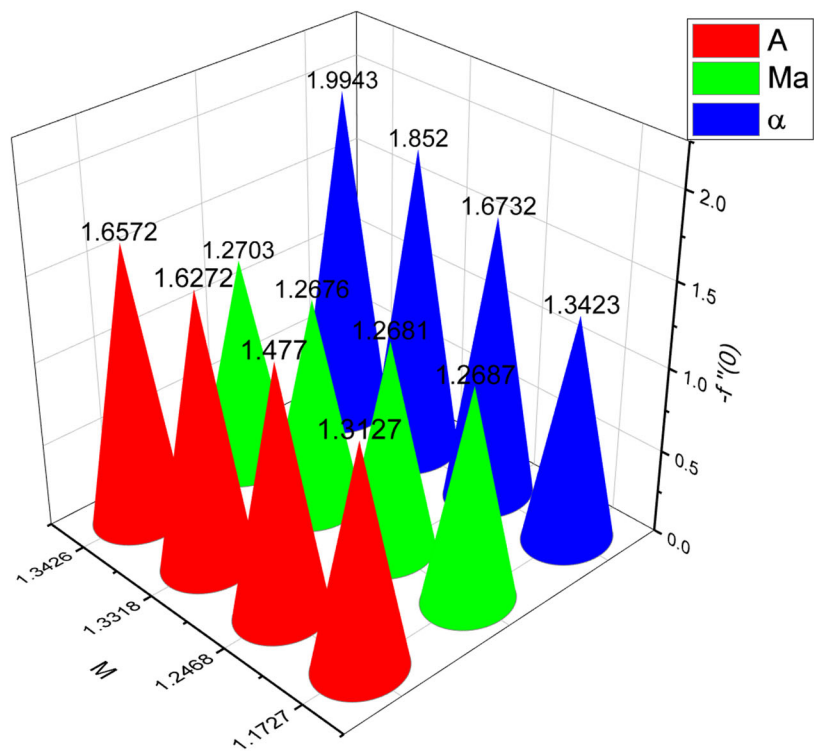


Figure 16. Skin friction estimation via (M, a, Ma, α) parameters.

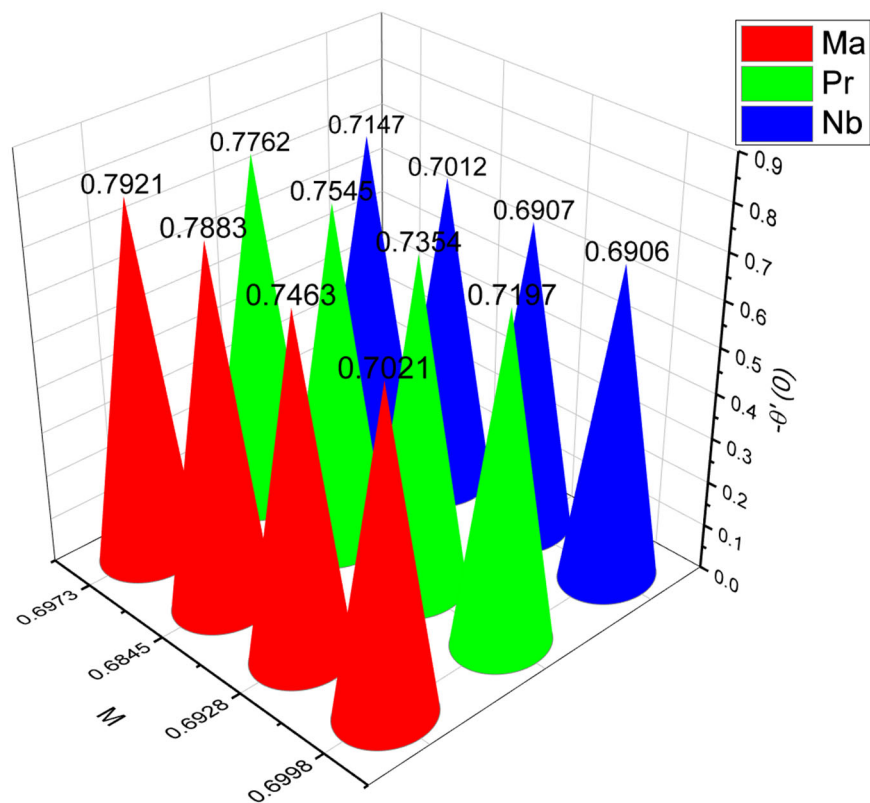


Figure 17. Heat transfer estimation via (M, Ma, Pr, Nb) parameters.

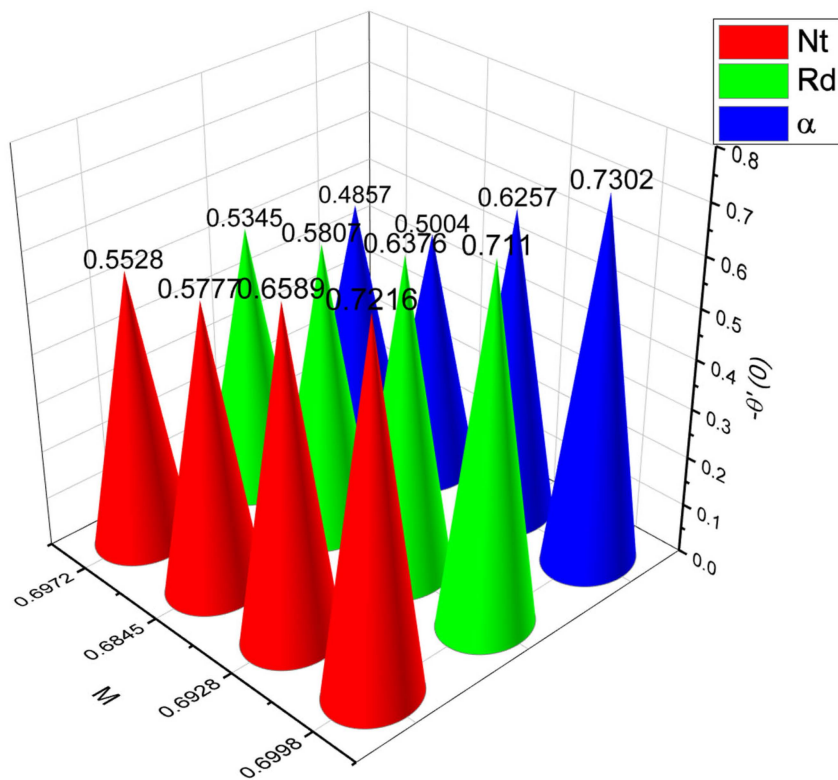


Figure 18. Heat transfer estimation via different physical parameters (M, Nt, Rd, α) .

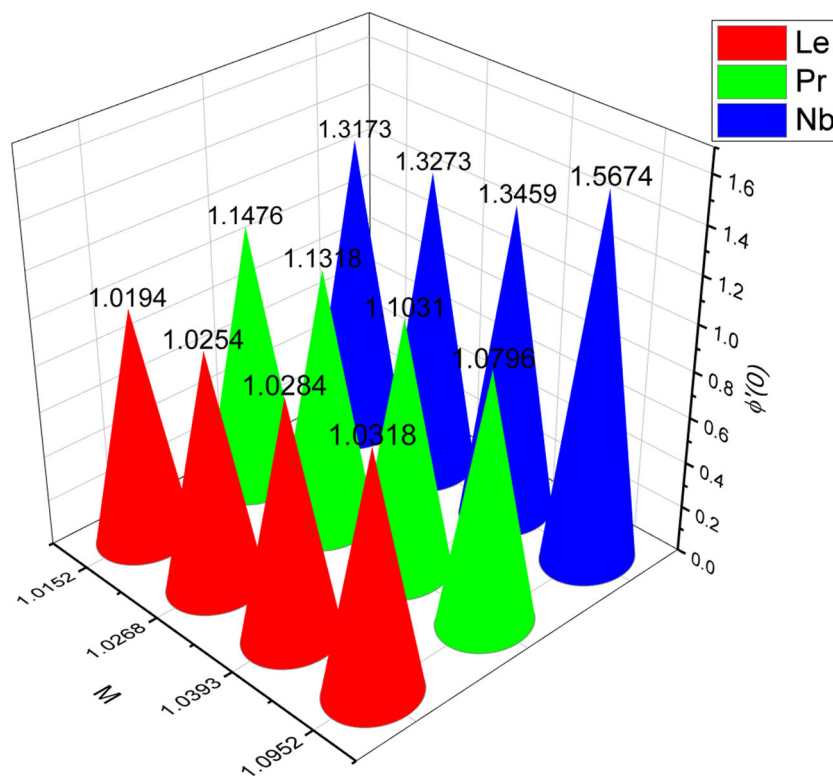


Figure 19. Mass flow rate estimation via different physical parameters (M, Le, Pr, Nb).

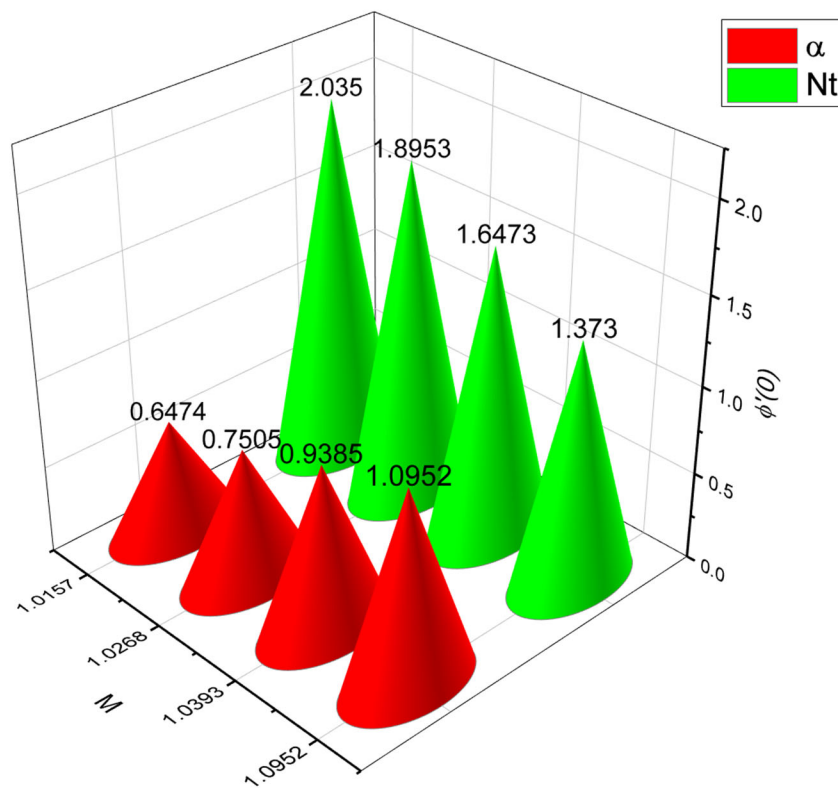


Figure 20. Mass flow rate estimation via different physical parameters (M, α, Nt).

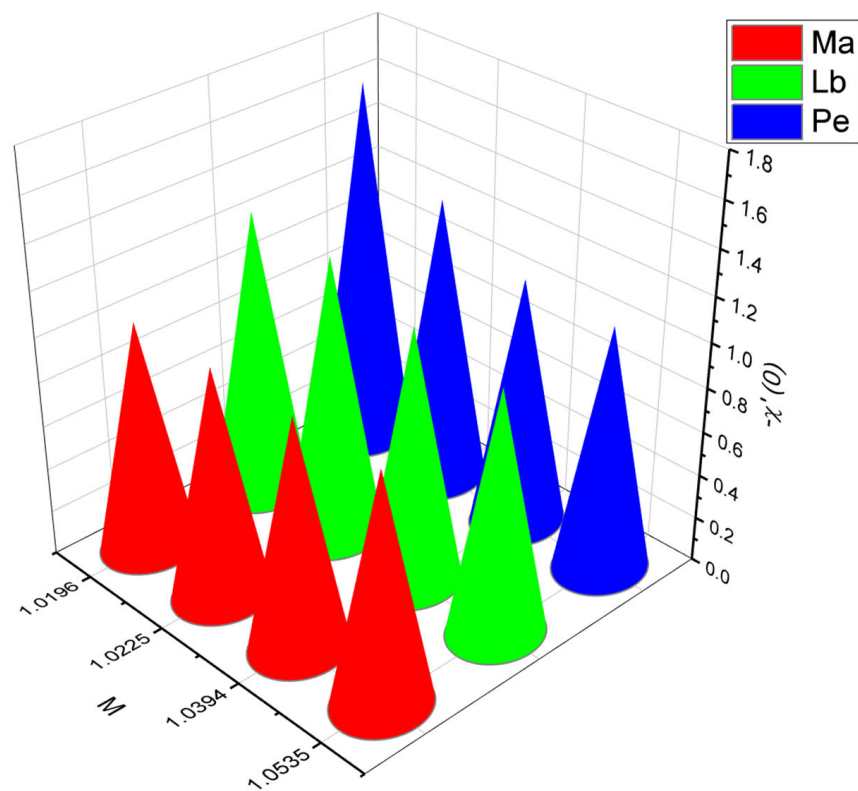


Figure 21. Microorganism estimation via different physical parameters (M, Ma, Lb, Pe).

Figure 2a explains the effects of varying values for the Re on the $u'_0(\zeta)$ profiles. With increasing values for the Re , the resulting reduction is witnessed in the $u'_0(\zeta)$ curves. Figure 2b elucidates the role of the (α) against the $u'_0(\zeta)$ field. Higher values for the (α) cause a decline in the flow stream as well as the boundary-layer thickness. Figure 3a sketches the impact of the (Ma) on the $u'_0(\zeta)$. The velocity boundary layer experiences upsurges when subjected to increasing values for the (Ma) parameter. The effects of the (λ) on the $u'_0(\zeta)$ profile are explained in Figure 3b. The velocity is increased with increasing values for the (λ) . Figure 4a demonstrates the effects of the (M) for various streams of fluid. Physically, this figure describes how increasing values for the (M) cause obstructions in the fluid flow profile. This retardation in the velocity field is due to the Lorentz forces, which are resistive in nature and are included in the magnetic parameter and react as a retarding force. As the magnetic effect boosts up, the Lorentz force is developed, which acts against the flow of fluid, causing the velocity patterns to decline. On the other hand, Figure 4b displays the effective correlation between the flow profile and the (Nc) parameter. One can observe how, with increasing values for the (Nc) parameter, the velocity field of the nanofluid decreases. Figure 5a presents the influence of the (We) on velocity function. The velocity distribution diminishes with increasing values for the (We) . Physically, the velocity function dwindles for different values for the (We) because an increase in the (We) means an increase in internal forces, which decreases fluid flow within the channel. The impacts of the (Nr) on the $u'_0(\zeta)$ profile are established in Figure 5b; it can be detected that with increasing values for the (Nr) parameter, the $u'_0(\zeta)$ field declines, and maximum velocity is attained at $(Nr = 0.1)$ while minimum velocity is achieved at the maximum value $(Nr = 1.3)$ for the buoyancy ratio parameter. From Figure 6a, it can be discerned that the energy gradient $g(\zeta)$ upturns by increasing the (Nt) . In reality, this phenomenon occurs due to the fact that high-energy worm nanoparticles are drawn away from the heated stretching surface and towards the colder regions by the thermophoretic diffusion effect, triggering an upsurge in the internal heating inside the thermal boundary-layer curves. Figure 6b explains the result of the (θ_w) on the energy gradient $g(\zeta)$ of the fluid profile.

It can be seen that an increase in the (θ_w) raises the thermal field distribution. Figure 7a describes the effect of the (Bi) on the energy profile $g(\zeta)$. Here, higher values for the (Bi) result in high convective transfer of heat in the fluid nanoparticles. Consequently, the energy field curves increase due to the increase in (Bi) , which results in massive convective heat transfer being observed. Physically, the (Bi) is related to the coefficient of heat transfer. Therefore, $g(\zeta)$ increases, as does associated layer thickness. The effects of increasing values for the conductivity factor (ε) on the energy $g(\zeta)$ profile is characterized in Figure 7b. Here, the energy gradient of the fluid intensifies for increasing values for the (ε) . Physically, extra heat is added to the nanofluid with increased values for the (ε) . Figure 8a,b show the profiles of the melting parameter (Ma) and (α) fluid temperature gradient. It can be seen from these profiles that increasing values for these parameters increase the internal energy of the fluid. Consequently, the $g(\zeta)$ increases. The effects of the (Pr) on fluid energy gradient $g(\zeta)$ distribution are illustrated in Figure 9a. Here, it can be seen that the energy profile $g(\zeta)$ decreases with higher values for the (Pr) . Physically, the (Pr) is defined as the ratio of thermal conductivity to thermal diffusivity of a fluid. Increasing values for the (Pr) cause minimum thermal diffusivity behavior of the nanofluid. Consequently, the $g(\zeta)$ and related thermal layer thickness deteriorate. The effects of the (λ) on the energy profile $g(\zeta)$ are plotted in Figure 9b. As can be seen, the energy profile of the nanofluid diminishes with higher (λ) values. Figure 10a reveals the (Nt) parameter impact on the $h(\zeta)$. Here, the nanoparticles concentration profile increases with higher (Nt) values. From a physical perspective, an increase in the thermophoretic diffusion force is perceived with increasing values for the (Nt) , which often moves the fluid molecules from a higher temperature region towards a lower one. Figure 10b describes the effect of the (Le) number on the $h(\zeta)$ profile when the default parameters are fixed. For diversified values for the (Le) number, the (Le) causes the decline of the $h(\zeta)$ profiles. Physically, higher values cause a rapid decline in diffusivity. Thus, the $h(\zeta)$ profiles decrease. Figure 11a explains the effect of the Brownian parameter on $h(\zeta)$. Evidently, an increment in the (Nt) magnitude increases the velocity with which fluid particles move at various speeds in different directions owing to the (Nt) aspect. As a result, larger Brownian values create a decline in the $h(\zeta)$ and the associated concentration layer thickness. Figure 11b portrays the effect of the (ε_1) on the $h(\zeta)$. Here, the nanoparticles concentration profile increases with increasing values for the (ε_1) . Figure 12a,b illustrate the effects of the (Ma) and (α) on the $h(\zeta)$ profiles. As can be seen, the concentration of nanoparticles is enhanced with increasing values for the (Ma) . Thus, the effect of the melting parameter on the $h(\zeta)$ depends on a number of factors, including nanoparticle size, shape, and surface chemistry, as visualized in Figure 12a. The concentration profile of the nanoparticles is improved for greater values of the (α) , as shown in Figure 12b.

Figure 13a illustrates how the distribution of motile swimming microbes, denoted as $X(\zeta)$, is affected by the (Lb) number. As can be seen, as the (Lb) number increases, the thickness of the $X(\zeta)$ profile declines for both the shear thickening and the shear thinning cases. On the other hand, Figure 13b displays the effect of the (Pe) number on the distribution of living microbes profile. When the dimensionless parameter increases, the motile swimming outlook $X(\zeta)$ declines relative to the increasing values of the (Pe) number. The motile swimming microbes profile $X(\zeta)$ is depicted in Figure 14a,b to exemplify the characteristics of the (α) and (Ma) parameters. It can be seen that the motility of the living microbes enhances as the (α) parameter increases. Furthermore, the swimming profiles increase as the (Ma) parameter becomes larger.

Figures 15 and 16 are included to elucidate the role of the drag force coefficient for various physical parameters, namely, the (Nr) , (Nr) , (α) , (A) , and (Ma) , respectively. From these visuals, it is clear that the surface drag force coefficient increases with higher values for these parameters, while decreasing with increasing values of the (λ) . Figures 17 and 18 explain the impact of important physical constraints on the heat transfer rate coefficient. The heat flow rate increases with increasing values for the physical parameters. Figures 19 and 20 exhibit the variation in the mass flow rate coefficient as a result

of different parameters. It can be seen that an increase in the response of the flow rate of mass occurs when the (Pr) number and the (Nt) parameter are increased from low-level to high-level values. The way that the mass flow coefficient decreases significantly with a change from low-level to higher-level values for the (Le) number, (Nb) , and (α) is highlighted through these visuals. Also displayed here, in Figure 21, is the local microorganism number. From Figure 21, it can clearly be seen that the microorganism number increases with higher values for the (Ma) , (Lb) number, and (Pe) number.

5. Closing Points

This study investigated the characteristics of MHD bioconvection flow of nanofluid in the presence of melting heat transfer rheology and expanded the analysis by implementing the swimming microbes model for heat and mass flow rate. Additionally, a homotopic scheme was employed to obtain the nonlinear computational results of the ODEs acquired through similarity transformations of the resulting PDEs. The computational results so acquired were correlated with the results obtained in previously published studies, and a reasonable degree of agreement was established, hence authenticating the nonlinear solution. The principal outcomes of the current study are summarized below:

- The velocity field of bio-nanofluid flow rises as the values for the (α) and (Ma) parameters are increased; however, the velocity profile reduces with increasing values for the (We) , (M) , and (α) parameters.
- The fluid energy profile decreases with increased values for the (α) parameter and the (Le) number but increases with increases in the (Ma) , (Nt) , and thermal (Bi) number.
- With increased values for the (Nt) parameter, (ε) , and (α) , the concentric layer thickness increases. On the other hand, for increased values for the (Le) and (Nb) dispersion effect, the concentration profile decreases.
- Increasing values for the (Lb) and (Pe) numbers considerably suppress the density profile of living microbes, whereas the (α) and (Ma) parameters boost the motile density of microorganism profile.
- The surface drag force coefficient reduces with higher values for the (λ) , but it increases when the (Nc) and (α) parameters are increased.
- The mass flow rate increases when the (Pr) number as well as the (Nt) parameter increase. On the other hand, it decreases when the (Nb) parameter and the (Le) number increase.

Future work: The Cross nanofluid was used in the present model. The same model can be extended by using the other non-Newtonian fluids, biofluids. The concepts of variable viscosity and variable thermal conductivity are also possibilities for future work.

Author Contributions: Conceptualization, F.A.A. and E.A.A.I.; Methodology, T.G.; Software, I.A.; Writing—Original draft; Preparation, T.G. and W.K.; Writing—Review and Editing, T.G. and W.K.; Project administration, F.A.A. and E.A.A.I.; Funding acquisition, F.A.A. and E.A.A.I. All authors have read and agreed to the published version of the manuscript.

Funding: Project number (RSPD2023R576), King Saud University, Riyadh, Saudi Arabia.

Data Availability Statement: The datasets used and/or analyzed during the current study are available from the corresponding author on reasonable request.

Acknowledgments: Researchers Supporting Project number (RSPD2023R576), King Saud University, Riyadh, Saudi Arabia.

Conflicts of Interest: The authors declare no conflict of interest.

Nomenclature

V	velocity
T_{∞}^*	ambient temperature
C_{∞}^*	nanoparticle volume fraction
N_{∞}^*	motile microorganisms
α	curvature parameter
M	magnetic parameter
A	time-dependent parameter
Nr	buoyancy parameter
Nc	Rayleigh number
λ	convection parameter
We	Weissenberg number
Pr	Prandtl number
R	radiation parameter
Nb	Brownian factor
Nt	thermophoretic force
θ_w	ratio parameter
Le	Lewis number
Lb	bioconvection Lewis number
Pe	Peclet number
Ma	melting heat phenomenon
Bi	Biot number
$\tau_{x^*r^*}$	elucidates shear stress
q_w	heat flux
q_m	mass flux
q_j	mass of living microbes
Cf	skin fraction
Nu	heat transfer coefficient
Sh	mass flow rate
Nh	gradients of living microbes
Re_x	local Reynolds number

References

- Choi, S.U.S. Enhancing thermal conductivity of fluids with nanoparticles, development and applications of non-Newtonian flows. *Fluids Eng. Div.* **1995**, *231*, 99–110.
- Narsimulu, K.; Gopal, D.; Udaikumar, R. Numerical approach for enhanced mass transfer of Bio-convection on Magneto-hydrodynamic Carreau fluid flow through a nonlinear stretching surface. *Mater. Today Proc.* **2022**, *49*, 2267–2275. [[CrossRef](#)]
- Imran, M.; Kamran, T.; Khan, S.A.; Muhammad, T.; Waqas, H. Physical attributes of bio-convection in nanofluid flow through a paraboloid of revolution on horizontal surface with motile microorganisms. *Int. Commun. Heat Mass Transf.* **2022**, *133*, 105947. [[CrossRef](#)]
- Waqas, H.; Khan, S.A.; Khan, S.U.; Khan, M.I.; Kadry, S.; Chu, Y.M. Falkner-Skan time-dependent bioconvection flow of cross nanofluid with nonlinear thermal radiation, activation energy and melting process. *Int. Commun. Heat Mass Transf.* **2021**, *120*, 105028. [[CrossRef](#)]
- Yahya, A.U.; Salamat, N.; Habib, D.; Ali, B.; Hussain, S.; Abdal, S. Implication of Bio-convection and Cattaneo-Christov heat flux on Williamson Sutterby nanofluid transportation caused by a stretching surface with convective boundary. *Chin. J. Phys.* **2021**, *73*, 706–718. [[CrossRef](#)]
- Buongiorno, J. Convective transport in nanofluid. *J. Heat Transf.* **2006**, *128*, 240–250. [[CrossRef](#)]
- Venkatahari, K.; Gaffar, S.A.; Rajarajeswari, P.; Prasad, V.R.; Anwar, B.O.; Hidayathulla, K.B.M. Melting heat transfer analysis of electrically conducting nanofluid flow over an exponentially shrinking/stretching porous sheet with radiative heat flux under a magnetic field. *Heat Transf.* **2020**, *49*, 4281–4303. [[CrossRef](#)]
- Mondal, H.; Bharti, S. Spectral Quasi-linearization for MHD nanofluid stagnation boundary layer flow due to a stretching/shrinking surface. *J. Appl. Comput. Mech.* **2020**, *6*, 1058–1068.
- Ying, Z.; He, B.; Su, L.; Kuang, Y.; He, D.; Lin, C. Convective heat transfer of molten salt-based nanofluid in a receiver tube with non-uniform heat flux. *Appl. Therm. Eng.* **2020**, *181*, 115922. [[CrossRef](#)]
- Zainal, N.A.; Nazar, R.; Naganthran, K.; Pop, I. Stability analysis of MHD hybrid nanofluid flow over a stretching/shrinking sheet with quadratic velocity. *Alex. Eng. J.* **2020**, *60*, 915–926. [[CrossRef](#)]
- Eid, M.R.; Nafe, M.A. Thermal Conductivity Variation and Heat Generation Effects on Magneto-Hybrid Nanofluid Flow in a Porous Medium with Slip Condition. *Waves Random Complex Media* **2020**, *32*, 1103–1127. [[CrossRef](#)]

12. Alharbi, S.O.; Gul, T.; Khan, I.; Khan, M.S.; Alzahrani, S. Irreversibility Analysis through Neural Networking of the Hybrid Nanofluid for the Solar Collector Optimization. *Sci. Rep.* **2023**, *13*, 13350. [[CrossRef](#)] [[PubMed](#)]
13. Khan, N.; Hashmi, M.S.; Khan, S.U.; Chaudhry, F.; Tlili, I.; Shadloo, M.S. Effects of homogeneous and heterogeneous chemical features on Oldroyd-B fluid flow between stretching disks with velocity and temperature boundary assumptions. *Math. Probl. Eng.* **2020**, *2020*, 5284906. [[CrossRef](#)]
14. Gul, T.; Mukhtar, S.; Alghamdi, W.; Raizah, Z.; Alhazmi, S.E.; El Din, E.T. Radiative couple stress Casson hybrid nanofluid flow over an inclined stretching surface due to nonlinear convection and slip boundaries. *Front. Energy Res.* **2022**, *10*, 965309. [[CrossRef](#)]
15. Al-Mubaddel, F.S.; Farooq, U.; Al-Khaled, K.; Hussain, S.; Khan, S.U.; Aijaz, M.O.; Waqas, H. Double stratified analysis for bioconvection radiative flow of Sisko nanofluid with generalized heat/mass fluxes. *Phys. Scr.* **2021**, *96*, 055004. [[CrossRef](#)]
16. Waqas, H.; Farooq, U.; Naseem, R.; Hussain, S.; Alghamdi, M. Impact of MHD radiative flow of hybrid nanofluid over a rotating disk. *Case Stud. Therm. Eng.* **2021**, *26*, 101015. [[CrossRef](#)]
17. Eshgarf, H.; Kalbasi, R.; Maleki, A.; Shadloo, M.S. A review on the properties, preparation, models and stability of hybrid nanofluids to optimize energy consumption. *J. Therm. Anal. Calorim.* **2020**, *144*, 1959–1983. [[CrossRef](#)]
18. Imran, M.; Farooq, U.; Muhammad, T.; Khan, S.U.; Waqas, H. Bioconvection transport of Carreau nanofluid with magnetic dipole and nonlinear thermal radiation. *Case Stud. Ther. Eng.* **2021**, *26*, 101129. [[CrossRef](#)]
19. Tlili, I.; Rabeti, M.; Shadloo, M.S.; Abdelmalek, Z. Forced convection heat transfer of nanofluids from a horizontal plate with convective boundary condition and a line heat source embedded in porous media. *J. Therm. Anal. Calorim.* **2020**, *141*, 2081–2094. [[CrossRef](#)]
20. Kamal, M.H.A.; Ali, A.; Shafie, S.; Rawi, N.A.; Ilias, M.R. G-Jitter effect on heat and mass transfer of 3-D stagnation point nanofluid flow with heat generation. *Ain Shams Eng. J.* **2020**, *11*, 1275–1294. [[CrossRef](#)]
21. Anuar, N.S.; Bachok, N.; Arifin, N.M.; Rosali, H. Numerical solution of stagnation point flow and heat transfer over a non-linear stretching/shrinking sheet in hybrid nanofluid: Stability analysis. *J. Adv. Res. Fluid Mech. Therm. Sci.* **2020**, *76*, 85–98. [[CrossRef](#)]
22. Rizwana, R.; Hussain, A.; Nadeem, S. Slip Effects on Unsteady Oblique Stagnation Point Flow of Nanofluid in a View of Inclined Magnetic Field. *Math. Probl. Eng.* **2020**, *2020*, 6580409. [[CrossRef](#)]
23. Giri, S.S.; Das, K.; Kundu, P.K. Influence of nanoparticle diameter and interfacial layer on magnetohydrodynamic nanofluid flow with melting heat transfer inside rotating channel. *Math. Methods Appl. Sci.* **2020**, *44*, 1161–1175. [[CrossRef](#)]
24. Sharma, R.P.; Acharya, N.; Das, K. On the Impact of Variable Thickness and Melting Transfer of Heat on Magnetohydrodynamics Nanofluid Flow Past a Slandering Stretching Sheet. *Indian J. Geo-Mar. Sci.* **2020**, *49*, 641–648.
25. Platt, J.R. Bioconvection patterns' in cultures of free swimming organisms. *Science* **1961**, *133*, 1766–1767. [[CrossRef](#)] [[PubMed](#)]
26. Kuznetsov, A.V. Nanofluid bioconvection in water-based suspensions containing nanoparticles and oxytactic microorganisms: Oscillatory instability. *Nanoscale Res. Lett.* **2011**, *6*, 100. [[CrossRef](#)] [[PubMed](#)]
27. Kuznetsov, A.V. Non-oscillatory and oscillatory nanofluid bio-thermal convection in a horizontal layer of finite depth. *Eur. J. Mech. B Fluid* **2010**, *30*, 156–165. [[CrossRef](#)]
28. Haq, F.; Saleem, M.; Rahman, M.U. Investigation of natural bio-convective flow of Cross nanofluid containing gyrotactic microorganisms subject to activation energy and magnetic field. *Phys. Scr.* **2020**, *95*, 105219. [[CrossRef](#)]
29. Ahmad, S.; Ashraf, M.; Ali, K. Nanofluid flow comprising gyrotactic microorganisms through a porous medium. *J. Appl. Fluid Mech.* **2020**, *13*, 1539–1549.
30. Elanchezhian, E.; Nirmalkumar, R.; Balamurugan, M.; Mohana, K.; Prabu, K.M.; Vilorio, A. Heat and mass transmission of an Oldroyd-B nanofluid flow through a stratified medium with swimming of motile gyrotactic microorganisms and nanoparticles. *J. Therm. Anal. Calorim.* **2020**, *14*, 2613–2623. [[CrossRef](#)]
31. Bhatti, M.M.; Marin, M.; Zeeshan, A.; Ellahi, R.; Abdelsalam, S.I. Swimming of motile gyrotactic microorganisms and nanoparticles in blood flow through anisotropically tapered arteries. *Front. Phys.* **2020**, *8*, 95. [[CrossRef](#)]
32. Khan, S.U.; Tlili, I. Significance of activation energy and effective Prandtl number in accelerated flow of Jeffrey nanoparticles with gyrotactic microorganisms. *J. Energy Resour. Technol.* **2020**, *142*, 112101. [[CrossRef](#)]
33. Shafiq, A.; Rasool, G.; Khaliq, C.M.; Aslam, S. Second grade bioconvective nanofluid flow with buoyancy effect and chemical reaction. *Symmetry* **2020**, *12*, 621. [[CrossRef](#)]
34. Kotnurkar, A.S.; Katagi, D.C. Bioconvective Peristaltic Flow of a Third-Grade Nanofluid Embodying Gyrotactic Microorganisms in the Presence of Cu-Blood Nanoparticles with Permeable Walls. *Multidiscip. Model. Mater. Struct.* **2020**, *17*, 293–316. [[CrossRef](#)]
35. Muhammad, T.; Alamri, S.Z.; Waqas, H.; Habib, D.; Ellahi, R. Bioconvection flow of magnetized Carreau nanofluid under the influence of slip over a wedge with motile microorganisms. *J. Therm. Anal. Calorim.* **2020**, *143*, 945–957. [[CrossRef](#)]
36. Farooq, U.; Waqas, H.; Khan, M.I.; Khan, S.U.; Chu, Y.M.; Kadry, S. Thermally radioactive bioconvection flow of Carreau nanofluid with modified Cattaneo-Christov expressions and exponential space-based heat source. *Alex. Eng. J.* **2021**, *60*, 3073–3086. [[CrossRef](#)]
37. Hosseinzadeh, K.; Roghani, S.; Mogharrebi, A.R.; Asadi, A.; Waqas, M.; Ganji, D.D. Investigation of cross-fluid flow containing motile gyrotactic microorganisms and nanoparticles over a three-dimensional cylinder. *Alex. Eng. J.* **2020**, *59*, 3297–3307. [[CrossRef](#)]

38. Algehyne, E.A.; Ahammad, N.A.; Elnair, M.E.; Zidan, M.; Alhusayni, Y.Y.; El-Bashir, B.O.; Alzahrani, F. Enhancing Heat Transfer in Blood Hybrid Nanofluid Flow with Ag–TiO₂ Nanoparticles and Electrical Field in a Tilted Cylindrical W-Shape Stenosis Artery: A Finite Difference Approach. *Symmetry* **2023**, *15*, 1242. [[CrossRef](#)]
39. Loganathan, K.; Eswaramoorthi, S.; Chinnasamy, P.; Jain, R.; Sivasakthivel, R.; Ali, R.; Devi, N.N. Heat and Mass Transport in Casson Nanofluid Flow over a 3-D Riga Plate with Cattaneo-Christov Double Flux: A Computational Modeling through Analytical Method. *Symmetry* **2023**, *15*, 725. [[CrossRef](#)]
40. Awwad, F.A.; Ismail, E.A.; Gul, T. Heat and Mass Transfer Gravity Driven Fluid Flow over a Symmetrically-Vertical Plane through Neural Networks. *Symmetry* **2023**, *15*, 1288. [[CrossRef](#)]
41. Sindhu, R.; Alessa, N.; Eswaramoorthi, S.; Loganathan, K. Comparative Analysis of Darcy–Forchheimer Radiative Flow of a Water-Based Al₂O₃-Ag/TiO₂ Hybrid Nanofluid over a Riga Plate with Heat Sink/Source. *Symmetry* **2023**, *15*, 199. [[CrossRef](#)]
42. Yusuf, T.A.; Mabood, F.; Prasannakumara, B.C.; Sarris, I.E. Magneto-bioconvection flow of williamson nanofluid over an inclined plate with gyrotactic microorganisms and entropy generation. *Fluid* **2021**, *6*, 109. [[CrossRef](#)]
43. Gireesha, B.J.; Shankaralingappa, B.M.; Prasannakumar, B.C.; Nagaraja, B. MHD flow and melting heat transfer of dusty Casson fluid over a stretching sheet with Cattaneo–Christov heat flux model. *Int. J. Ambient Energy* **2020**, *43*, 2931–2939. [[CrossRef](#)]
44. Alazwari, M.A.; Safaei, M.R. Combination effect of baffle arrangement and hybrid nanofluid on thermal performance of a shell and tube heat exchanger using 3-D homogeneous mixture model. *Mathematics* **2021**, *9*, 881. [[CrossRef](#)]
45. Ali, I.; Gul, T.; Khan, A. Unsteady Hydromagnetic Flow over an Inclined Rotating Disk through Neural Networking Approach. *Mathematics* **2023**, *11*, 1893. [[CrossRef](#)]
46. Rasheed, H.U.; Zeeshan; Islam, S.; Ali, B.; Shah, Q.; Ali, R. Implementation of shooting technique for Buongiorno nanofluid model driven by a continuous permeable surface. *Heat Transf.* **2023**, *52*, 119–3134. [[CrossRef](#)]
47. Atashafrooz, M.; Sajjadi, H.; Delouei, A.A. Interacting influences of Lorentz force and bleeding on the hydrothermal behaviors of nanofluid flow in a trapezoidal recess with the second law of thermodynamics analysis. *Int. Commun. Heat Mass Transf.* **2020**, *110*, 104411. [[CrossRef](#)]
48. Khan, W.A.; Ali, M.; Shahzad, M.; Sultan, F.; Irfan, M.; Asghar, Z. A note on activation energy and magnetic dipole aspects for Cross nanofluid subjected to cylindrical surface. *Appl. Nanosci.* **2020**, *10*, 3235–3244. [[CrossRef](#)]

Disclaimer/Publisher’s Note: The statements, opinions and data contained in all publications are solely those of the individual author(s) and contributor(s) and not of MDPI and/or the editor(s). MDPI and/or the editor(s) disclaim responsibility for any injury to people or property resulting from any ideas, methods, instructions or products referred to in the content.